THE STRUCTURE OF SPIRAL SHOCKS EXCITED BY PLANETARY-MASS COMPANIONS

Zhaohuan Zhu[1,4], Ruobing Dong[2,3,4], James M. Stone[1], and Roman R. Rafikov[1]
Draft version July 15, 2015

ABSTRACT

Recent high-resolution direct imaging observations have revealed spiral structure in protoplanetary disks. Previous studies have suggested that planet-induced spiral arms cannot explain these spiral patterns, as 1) the pitch angle of the spiral arm is larger in observations than that predicted by the linear density wave theory, 2) the contrast of the spiral arm is higher in observations than suggested by the synthetic observations based on two dimensional planet-disk simulations. We have carried out three dimensional (3-D) hydrodynamical simulations to study spiral wakes/shocks excited by young planets. We find that, in contrast with linear theory, the pitch angle of spiral arms does depend on the planet mass, which can be explained by the non-linear density wave theory. The more massive is the planet, the larger pitch angle the spiral arm has, since a more massive planet excites a stronger shock which propagates considerably faster than the sound speed. A secondary spiral arm, especially for the inner arms, is also excited by a massive planet. The more massive is the planet, the larger is the separation in the azimuthal direction between the primary and secondary arms. We also find that although the arms in the outer disk do not exhibit much vertical motion, the inner arms have significant vertical motion, which boosts the density perturbation at the disk atmosphere by more than a factor of 10 compared with that at the disk midplane. Combining hydrodynamical models with Monte-Carlo radiative transfer calculations, we find that the inner spiral arms are considerably more prominent in synthetic near-IR images using full 3-D hydrodynamical models than images based on 2-D models assuming vertical hydrostatic equilibrium, indicating the need to model observations with full 3-D hydrodynamics. Overall, spiral arms (especially inner arms) excited by planetary-mass objects are prominent features that are observable by current near-IR imaging facilities, and the shape of the spiral arms informs us not only about the position but also about the mass of the companion.

Subject headings: accretion, accretion disks - planet-disk interaction - protoplanetary disks - stars: protostars

1. INTRODUCTION

Recent high-resolution direct imaging observations have revealed spiral structure in several protoplanetary disks around Herbig Ae/Be stars, such as SAO 206462 (Muto et al. 2012; Garufi et al. 2013) and MWC 758 (Grady et al. 2013; Benisty et al. 2015). The polarized intensity has been measured in these observations to gain higher contrast between the disk and the central star. While the thermal emission from the central star is unpolarized, the scattered light from the disk is polarized. In these near-infrared (near-IR) polarized intensity images, two spiral arms with roughly 180° rotational symmetry are normally present, similar to the grand design in a spiral galaxy (e.g. the Whirlpool Galaxy M51). The spiral arms also exhibit a high contrast against the background disk. The polarized intensity of the spiral arm is several times higher than that of the region outside the spiral arm. It should also be noted that, since the dust scattering opacity is quite large, these observations only probe structure high up at the disk atmosphere (e.g. several disk scale heights) where the last dust scattering surface is.

In addition to spiral patterns, these disks also have gaps or holes, which indicates they are members of the protoplanetary disk class called transitional disks (Espaillat et al. 2014). One scenario to explain both spiral patterns and gaps/holes is that these disks harbor low-mass companions (e.g. young planets) which can open gaps and excite spiral waves at the same time (e.g., Baruteau et al. 2014).

However, there are two difficulties in explaining the observed spiral patterns using planet-induced spiral wakes. First, the large pitch angle of the observed spiral arms suggests that the disk has a relative high temperature ($\sim$250 K at 70 AU, Benisty et al. 2015). In linear theory, spiral waves are basically sound waves in disks, and the pitch angle of the spiral arms is directly related to the sound speed in the disk. Using the linear theory, the best fit models for both SAO 206462 (Muto et al. 2012) and MWC 758 (Grady et al. 2013; Benisty et al. 2015) suggest that the disk aspect ratio (H/R with $H \equiv c_s/\Omega$) at $R \sim 100$ AU is around 0.2 which is too large for any realistic disk structure. For example, even if the stellar irradiation is perpendicular to the disk surface [5], the maximum disk temperature due to the stellar irradiation is $\sigma T(R)^4 = L_*/4\pi R^2$. Assuming a 2 $M_\odot$ central star with 10 $L_\odot$ luminosity, the maximum temperature is $\sim$70 K at 100 AU and H/R is only $\sim$0.1. Since $H/R \propto L_*^{1/8}$ based on above relations, it is very difficult to make $H/R \sim$0.2.

zhzhu@astro.princeton.edu
[1] Department of Astrophysical Sciences, 4 Ivy Lane, Peyton Hall, Princeton University, Princeton, NJ 08544, USA
[2] Lawrence Berkeley National Lab, Berkeley, CA 94720, rdong2013@berkeley.edu
[3] Department of Astronomy, University of California at Berkeley, Berkeley, CA 94720
[4] Hubble Fellow.

[5] In reality, the stellar irradiation to the disk is not that efficient since the light from the star impinges very obliquely on the disk.

Second, the observed spiral arms exhibit much higher brightness contrasts than suggested by the synthetic observations based on two dimensional (2-D) planet-disk simulations. Juhász et al. (2015) have calculated the polarized scattered light images by combining 2-D hydrodynamical simulations with 3-D Monte-Carlo radiative transfer (MCRT) simulations. Vertical hydrostatic equilibrium has been assumed to extend the 2-D simulation to the third dimension (the vertical direction). They find that a relative change of about 3.5 on the spiral arms in the surface density is required for the spirals to be detectable. This value is a factor of eight higher than what is seen in their hydrodynamical simulations.

In this paper, we first point out that the pitch angle formula derived from the linear theory, which has been used in almost all previous spiral arm modeling efforts, does not apply to the high planet mass cases. Spiral wakes that are excited by high mass planets (e.g. 1 M_J) become spiral shocks which propagate at speeds faster than the local sound speed. The pitch angle difficulty above can be alleviated by considering the non-linear extension of the spiral shock theory. We also show that spiral arms (especially the inner arms) have complicated non-hydrostatic 3-D structure. Such structure can lead to strong density perturbation at the disk surface resulting in a corrugated shape of its atmosphere. Since near-IR observations only probe the shape of disk surface, this effect alleviates the second difficulty mentioned above. In Dong et al. (2015), we have combined MCRT simulations with hydrodynamical simulations from this paper and demonstrated that planet-induced inner spiral arms can explain recent near-IR direct imaging observations of SAO 206462 and MWC 758.

Before we introduce our numerical method in §3, we provide the theoretical background in §2. The shape of the spiral wakes will be studied in §4, and their 3-D structure will be presented in §5. After a short discussion in §6, we summarize our results in §7.

2. THEORETICAL BACKGROUND

As a result of planet-disk interaction, a spiral arm forms due to the constructive interference of density wakes with different azimuthal wavenumbers m excited by the planet at Lindblad resonances. In the linear density wave theory, the m-th Fourier component of the planet potential excites the density wave having m spiral arms

$$\delta(R, \phi, t) = \delta_0(R) e^{i[\int k_R(R)dR + m(\phi - \Omega_p t)]} \qquad (1)$$

where δ is any perturbed quantity associated with the wave, $\delta_0(R)$ is its complex amplitude, $k_R(R)$ is the radial wave vector, and Ω_p is the planet orbital frequency. Thus, the wave has the same phase along the curve satisfying $dR/d\phi = -m/k_R(R)$. The pitch angle (β) of the equal phase curve satisfies $\tan\beta = |dR/(Rd\phi)|$, so $\beta = \tan^{-1}|m/[k_R(R)R]|$. Using the dispersion relationship for density waves in the large m limit and far from the launching point, $m^2(\Omega(R) - \Omega_p)^2 \approx c_s^2 k_R(R)^2$, we have $\beta = \tan^{-1}[c_s/(R|\Omega(R) - \Omega_p|)]$. Because β is independent of m, different m modes can constructively interfere to form the one armed spiral wake (Ogilvie & Lubow 2002). If the equal phase curve is integrated from the planet's position (R_p, ϕ_p), the shape of the wake far from

R_p is given by Rafikov (2002) and Muto et al. (2012) as

$$\phi(R) = \phi_p - \frac{\mathrm{sgn}(R - R_p)}{h_p}$$
$$\times \left[\left(\frac{R}{R_p}\right)^{1+\beta} \left\{ \frac{1}{1+\beta} - \frac{1}{1 - \alpha + \beta} \left(\frac{R}{R_p}\right)^{-\alpha} \right\} \right.$$
$$\left. - \left(\frac{1}{1+\beta} - \frac{1}{1 - \alpha + \beta}\right) \right] \qquad (2)$$

where $h_p = H/R$ is the disk aspect ratio at R_p.

However, when the planet is massive enough, the above linear density wave theory breaks down. Linear waves excited by planets will steepen to shocks (Goodman & Rafikov 2001, Rafikov 2002, Dong, Rafikov & Stone 2012, Duffell & MacFadyen 2012, Zhu et al. 2013) after they propagate over a distance

$$|x_{sh}| \approx 0.93 \left(\frac{\gamma + 1}{12/5} \frac{M_p}{M_{th}}\right)^{-2/5} H \, . \qquad (3)$$

where γ is the adiabatic index, and M_{th} is the disk thermal mass

$$M_{th} \equiv \frac{c_s^3}{G\Omega_p} \approx 1 M_J \left(\frac{h_p}{0.1}\right)^3 \left(\frac{M_*}{M_\odot}\right) \, . \qquad (4)$$

When $M_p > M_{th}$, the spiral waves will immediately become spiral shocks after they are excited around the planet. Unlike the linear wake which follows Equation (2), the spiral shock will expand away from the trajectory predicted by Equation (2). Thus, if there is a massive planet in the disk, using Equation (2) to fit the shape of the spiral shocks will predict an incorrect disk aspect ratio and temperature.

3. NUMERICAL SIMULATIONS
3.1. *Method*

To study density wakes/shocks excited by planets, we have carried out both 2-D and 3-D numerical simulations using Athena++. Athena++ is a newly developed grid based code using a higher-order Godunov scheme for MHD and the constrained transport (CT) to conserve the divergence-free property for magnetic fields (Stone 2015). Compared with its predecessor Athena (Gardiner & Stone 2005, 2008; Stone et al. 2008), Athena++ is highly optimized and uses flexible grid structures, allowing global numerical simulations spanning a large radial range. Furthermore, the geometric source terms in curvilinear coordinates (e.g. in cylindrical and spherical coordinates) are carefully implemented so that angular momentum is conserved exactly (to machine precision), which makes the code ideal for global disk simulations.

Our simulations use the adiabatic equation of state (EoS) with the adiabatic index γ=1.4. A simple orbital cooling scheme has been applied to mimic the radiative cooling process in disks. In 3-D simulations, we have adopted

$$\frac{dE}{dt} = \frac{E - c_v \rho T_{irr}}{t_{cool}} \, , \qquad (5)$$

where E is the internal energy per unit volume, while in 2-D simulations, we have adopted

$$\frac{dE}{dt} = \frac{E - c_v \Sigma T_{irr}}{t_{cool}} \qquad (6)$$

where E is the internal energy per unit area. $c_v \equiv k/(\mu m_u(\gamma-1))$ is the heat capacity per unit mass, k is the Boltzmann constant, μ is the mean molecular weight, and m_u is the atomic mass unit. The cooling time t_{cool} can be written in the dimensionless form as $T_{cool} = t_{cool}\Omega(R)$. We fix T_{cool} to be a constant in each simulation. With this scheme, the disk temperature is relaxed to the background disk temperature (T_{irr}) determined by stellar irradiation. In our simulations, T_{irr} is set to be the initial disk temperature. In a realistic disk, the radiative cooling rate per unit area can be approximated by (Hubeny 1990)

$$\frac{dE}{dt} = \frac{16}{3}\sigma(T_c^4 - T_{irr}^4)\frac{\tau}{1+\tau^2}, \qquad (7)$$

where σ is the Stefan-Boltzmann constant, $\tau = (\Sigma/2)\kappa_R$ is the optical depth in the vertical direction, κ_R is the Rosseland mean opacity, and T_c is the midplane temperature. Assuming $E = c_v\Sigma T_c$ and using Equations (6) and (7), we can derive

$$t_{cool} = \frac{3\Sigma c_v}{16\sigma(T_c^2 + T_{irr}^2)(T_c + T_{irr})}\frac{1+\tau^2}{\tau}. \qquad (8)$$

Approximating the polynomial of T_c and T_{irr} in the denominator of Equation 8 with $[\max(T_c, T_{irr})]^3$ and assuming the central star is 1 $M_\odot$, we have

$$T_{cool} = 0.002\left(\frac{\Sigma}{10\mathrm{gcm}^{-2}}\right)\left(\frac{100\mathrm{AU}}{R}\right)^{1.5}\frac{(60\mathrm{K})^3}{[\max(T_c, T_{irr})]^3}$$
$$\times\frac{1+\tau^2}{\tau} \qquad (9)$$

We have carried out three sets of simulations with $T_{cool} = 10^{-5}$, 1, and 100. They are respectively labeled as ISO, T1, T2 at the end of their names in Table 1. Simulations with fast cooling ($T_{cool} = 10^{-5}$) are equivalent to locally isothermal simulations. Thus, we refer to these simulations as isothermal simulations in the rest of the paper. When the disk has a large surface density and $\tau \gg 1$ (e.g. at 1 AU), T_{cool} can increase dramatically. Thus we have carried out simulations with $T_{cool} = 1$ and 100. Results from simulations with $T_{cool} = 100$ are qualitatively similar to those with $T_{cool} = 1$. Thus, in most part of the paper, we only show results with $T_{cool} = 10^{-5}$ and 1.

We have also varied the planet mass to be 0.01, 1, and 6 M_J in our main set of simulations, which are labeled as M1, M2, and M3 in their names respectively. The thermal mass for the $h = 0.1$ disk around the solar mass star is $\sim M_J$. Thus, waves excited by a 0.01 M_J planet are in the linear regime and waves from a 6 M_J planet are in the highly non-linear regime. To compare with Figure 2 in Tanaka et al. (2002), we have also carried out a thin disk simulation with $H_p/R_p = 10^{-1.5}$ (STHIN in Table 1). The thermal mass for such a thin disk is only $M_{th} = 0.0316 \ M_J$. Thus, in order to ensure that the waves are in the linear regime, we choose the planet mass of $0.01M_{th} = 3.16 \times 10^{-4}M_J$ in this thin disk simulation. To avoid the divergence of planet potential, a smoothing length of 0.1 R_p has been applied for M2 and M3 cases. For the thin disk case which has a very small mass planet, we choose a smoothing length of $6\times10^{-3}R_p$, roughly the length of two grid cells. For the

low mass planet cases (M1), a smoothing length of 0.02 R_p, which is also roughly the length of two grid cells in these simulations, has been adopted. Planets are fixed in circular orbits at $R = 1$, and the indirect potential, which is due to the center of the coordinate system is at the star instead of the center of the mass, has been included. We have run the simulations for 10 planetary orbits. We choose this timescale because it is longer than the sound crossing time throughout the whole disk so that density waves/shocks have established, while it is shorter than the gap opening timescale to avoid complicated gap structures (e.g. vortices at the gap edges) and other longterm effects (e.g. radial buoyancy waves, Richert et al. 2015). Despite the short timescale of the simulation, the revealed wave mechanics should still hold in long terms, except that the wave amplitudes may decrease when gaps are carved out. Constant α viscosity with $\alpha = 10^{-4}$ has been applied. At inner and outer boundaries, all quantities are fixed at the initial states.

3.2. 2-D simulations

Compared with the 3-D simulations in the next subsection, 2-D simulations allow us to study density wakes in a bigger domain using a higher numerical resolution. The initial radial profile of the disk is

$$\Sigma(R, \phi) = \Sigma_0\left(\frac{R}{R_0}\right)^{-1} \qquad (10)$$

$$T(R, \phi) = T_0\left(\frac{R}{R_0}\right)^{-1/2}. \qquad (11)$$

We choose $\Sigma_0 = 1$, $R_0 = 1$, and $T_0 = 0.01$ to make $(H/R)_{R=1} = 0.1$.

Cylindrical coordinates have been adopted. To make every grid cell have equal length in the radial and azimuthal direction throughout the whole domain, the grids are uniformly spaced in $\log(R)$ from $R = 0.2$ to 10,

TABLE 1
MODELS

2-D				
Run	M_p M_J	T_{cool}	Domain R	Resolution $R \times \phi$
CM1ISO	0.01	10^{-5}	[0.2,10]	1280×2048
CM1T1	0.01	1	[0.2,10]	1280×2048
CM1T100	0.01	100	[0.2,10]	1280×2048
CM2ISO	1	10^{-5}	[0.2,10]	1280×2048
CM2T1	1	1	[0.2,10]	1280×2048
CM2T100	1	100	[0.2,10]	1280×2048
CM3ISO	6	10^{-5}	[0.2,10]	1280×2048
CM3T1	6	1	[0.2,10]	1280×2048
CM3T100	6	100	[0.2,10]	1280×2048

3-D				
Run	M_p M_J	T_{cool}	Domain $r \times \theta$	Resolution $r \times \theta \times \phi$
STHIN	0.000316	10^{-5}	$[0.5,2]\times[\frac{\pi}{2}\text{-}0.2,\frac{\pi}{2}\text{+}0.2]$	456×128×2048
SM1ISO	0.01	10^{-5}	$[0.3,3]\times[\frac{\pi}{2}\text{-}0.6,\frac{\pi}{2}\text{+}0.6]$	256×128×688
SM1T1	0.01	1	$[0.3,3]\times[\frac{\pi}{2}\text{-}0.6,\frac{\pi}{2}\text{+}0.6]$	256×128×688
SM1T100	0.01	100	$[0.3,3]\times[\frac{\pi}{2}\text{-}0.6,\frac{\pi}{2}\text{+}0.6]$	256×128×688
SM2ISO	1	10^{-5}	$[0.3,3]\times[\frac{\pi}{2}\text{-}0.6,\frac{\pi}{2}\text{+}0.6]$	256×128×688
SM2T1	1	1	$[0.3,3]\times[\frac{\pi}{2}\text{-}0.6,\frac{\pi}{2}\text{+}0.6]$	256×128×688
SM2T100	1	100	$[0.3,3]\times[\frac{\pi}{2}\text{-}0.6,\frac{\pi}{2}\text{+}0.6]$	256×128×688
SM3ISO	6	10^{-5}	$[0.3,3]\times[\frac{\pi}{2}\text{-}0.6,\frac{\pi}{2}\text{+}0.6]$	256×128×688
SM3T1	6	1	$[0.3,3]\times[\frac{\pi}{2}\text{-}0.6,\frac{\pi}{2}\text{+}0.6]$	256×128×688
SM3T100	6	100	$[0.3,3]\times[\frac{\pi}{2}\text{-}0.6,\frac{\pi}{2}\text{+}0.6]$	256×128×688

and uniformly spaced from 0 to 2π in the ϕ direction. Our standard resolution is 1280 in the R direction and 2048 in the ϕ direction, which is equivalent to 32 grids per H at $R = 1$ in both directions. In Table 1, 2-D runs are denoted with a "C" (cylindrical) in front of the model names, while 3-D runs are denoted with a "S" (spherical) in front of the model names.

3.3. 3-D simulations

To study the 3-D structure of density wakes/shocks, we have run 3-D hydrodynamical simulations in spherical polar coordinates. The initial density profile of the disk at the disk midplane is

$$\rho(R, z = 0) = \rho_0 \left(\frac{R}{R_0} \right)^p , \qquad (12)$$

and the temperature is constant on cylinders

$$T(R, z) = T_0 \left(\frac{R}{R_0} \right)^q . \qquad (13)$$

We want to emphasize that R should not be confused with r. In this paper, we use (R, ϕ, z) to represent positions in cylindrical coordinates while using (r, θ, ϕ) for spherical polar coordinates. ϕ represents the azimuthal direction (the direction of disk rotation) in both coordinate systems. Considering the disk structure is more natural to be described in cylindrical coordinates, we have transformed 3-D simulation results from spherical polar coordinates to cylindrical coordinates. Most results presented below are plotted in cylindrical coordinates with R representing the distance to the axis of the disk, even though the simulations are carried out in spherical polar coordinates.

Hydrostatic equilibrium in the $r - \theta$ plane requires that (e.g. Nelson et al. 2013)

$$\rho(R, z) = \rho_0 \left(\frac{R}{R_0} \right)^p \exp \left[\frac{GM}{c_s^2} \left(\frac{1}{\sqrt{R^2 + z^2}} - \frac{1}{R} \right) \right] , \qquad (14)$$

and

$$\Omega(R, z) = \Omega_K \left[(p + q) \left(\frac{H}{R} \right)^2 + (1 + q) - \frac{qR}{\sqrt{R^2 + z^2}} \right]^{1/2} , \qquad (15)$$

where $c_s = \sqrt{p/\rho}$ is the isothermal sound speed at R, $\Omega_K = \sqrt{GM_*/R^3}$, and $H = c_s/\Omega_K$ as defined before.

We choose $p = -2.25$ and $q = -1/2$ so that $\Sigma \propto R^{-1}$, similar to 2-D simulations above. H/R is 0.1 at $R=1$. The grids are uniformly spaced in $\log(r)$, θ, ϕ with $256 \times 128 \times 688$ grid cells in the domain of $[\log(0.3), \log(3)] \times [\pi/2-0.6, \pi/2+0.6] \times [0, 2\pi]$ for the main sets of simulations. In runs with $T_{cool} = 1$ and 100, the cooling time decreases exponentially beyond $z = 3H$ with $T_{cool}(z) = T_{cool}\exp(-(z^2/H^2 - 3^2))$ to mimic fast cooling at the disk surface. Numerically, this treatment also maintains better hydrostatic equilibrium at the disk surface.

The boundary condition in the θ direction is chosen that $v_r = v_\theta = 0$ in the ghost zones. We set v_ϕ and T in the ghost zones having the same values as the last active

zones. Density in the ghost zones is set to be

$$\rho(\theta_g) = \rho(\theta_a) \left| \frac{\sin(\theta_g)}{\sin(\theta_a)} \right|^{v_\phi^2/T} \qquad (16)$$

to maintain hydrostatic equilibrium in the θ direction, where θ_g and θ_a are the θ coordinates of the ghost and last active zones.

Volume rendering of $\delta\rho/\rho_0$ in simulation SM1ISO is shown in Figure 1. $\delta\rho$ is the density difference between 10 orbits and the initial condition, and ρ_0 is the initial density at that position. Thus, $\delta\rho/\rho_0$ highlights the density perturbation (e.g. spiral shocks) in the disk. In this paper, we use "spiral shocks" to refer to peaks of the density wakes and are associated with spiral arms seen in observations. It is apparent that the spiral shocks are not perpendicular to the disk midplane and they have complicated 3-D structure. Both the inner arms inside the planet and the outer arms outside the planet curl towards the central star at higher altitudes.

Such curled shocks in Figure 1, which are almost aligned with the θ direction in the spherical polar grid, make us suspect that they could be numerical artifacts due to the adopted grid structure. Thus, we have used Athena to carry out the same simulation but in cylindrical coordinates. We find the same curled shock structure in the Athena simulation. We have also calculated the eigenmodes from the Athena simulation using cylindrical grids and compare them with the eigenmodes from Athena++ simulations using spherical polar grids that will be presented in §5. Good agreements between Athena and Athena++ simulations have been achieved. This confirmation using another code with a different grid structure makes us confident that the results presented in this paper are robust.

4. THE SHAPE OF SPIRAL WAKES

When a very low mass planet is present in a disk, it excites density waves that are in the linear regime. The 2-D linear theory (Equation 2) can accurately describe the shape of the excited spiral wakes in 2-D simulations. This is demonstrated in the upper left panel (CM1ISO) of Figure 2 where Equation (2) fits the peak of the density wakes very well[6]. Even at the midplane of 3-D simulations, Equation (2) still provides a good fit to the density wakes (the upper middle panel).

However, the shape of the spiral arms at the disk surface is affected by the 3-D structure of density wakes. At the disk surface in 3-D simulations (even in the linear regime, shown in the upper right panel of Figure 2), both inner and outer arms are at smaller R than Equation (2) due to the tilted shock shape in Figure 1. When these shocks are far away from the planet, they are more tilted towards the central star at higher altitudes. This leads to the inner spiral arms becoming slightly more open (with a larger pitch angle) and the outer spiral arms becoming slightly less open (with a smaller pitch angle) than Equation (2) would predict.

When the planet has a mass larger than M_{th} (middle and bottom panels of Figure 2), it can launch spiral

---

[6] Strictly speaking, even with $M_p = 0.01M_J$ the excited density wakes become weak shocks at $R = 0.4$ and 1.6 according to Equation (3). But the shocks are very weak and do not move away from the trajectory predicted by Equation (2) significantly.
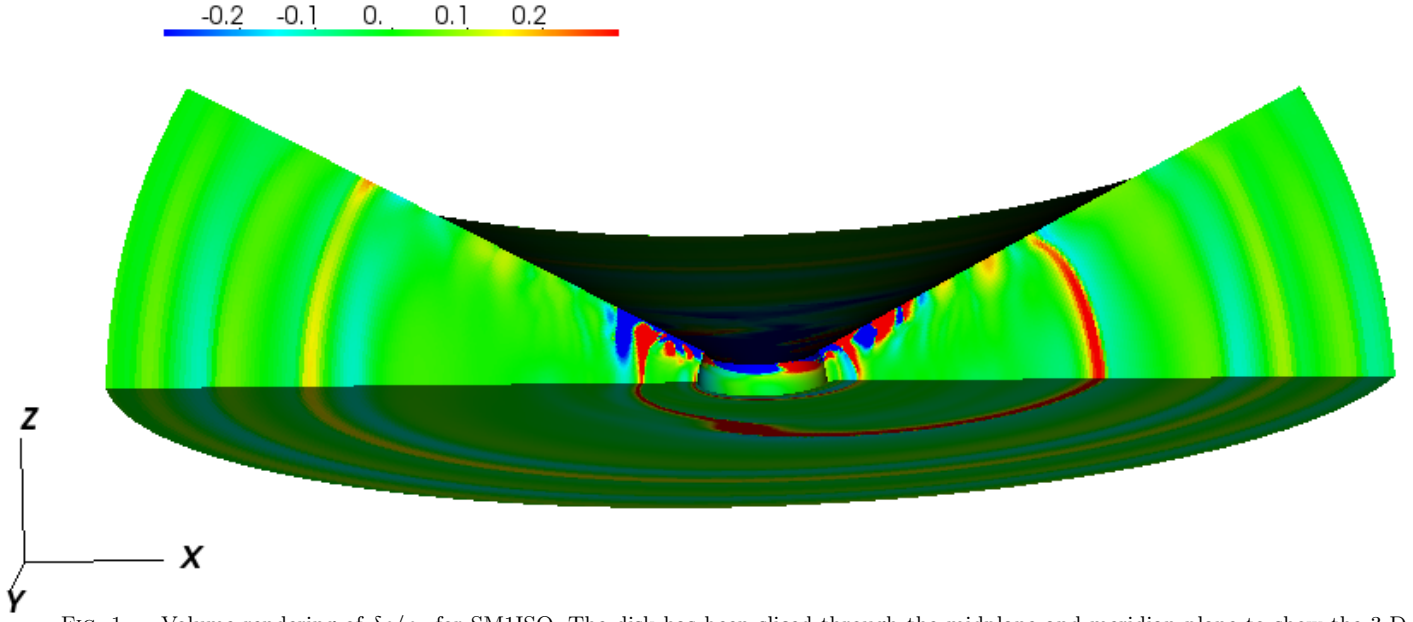
FIG. 1.— Volume rendering of $\delta\rho/\rho_0$ for SM1ISO. The disk has been sliced through the midplane and meridian plane to show the 3-D shock structure. Spiral shocks have been excited by the planet, and the shocks curl towards the central star at the disk surface.
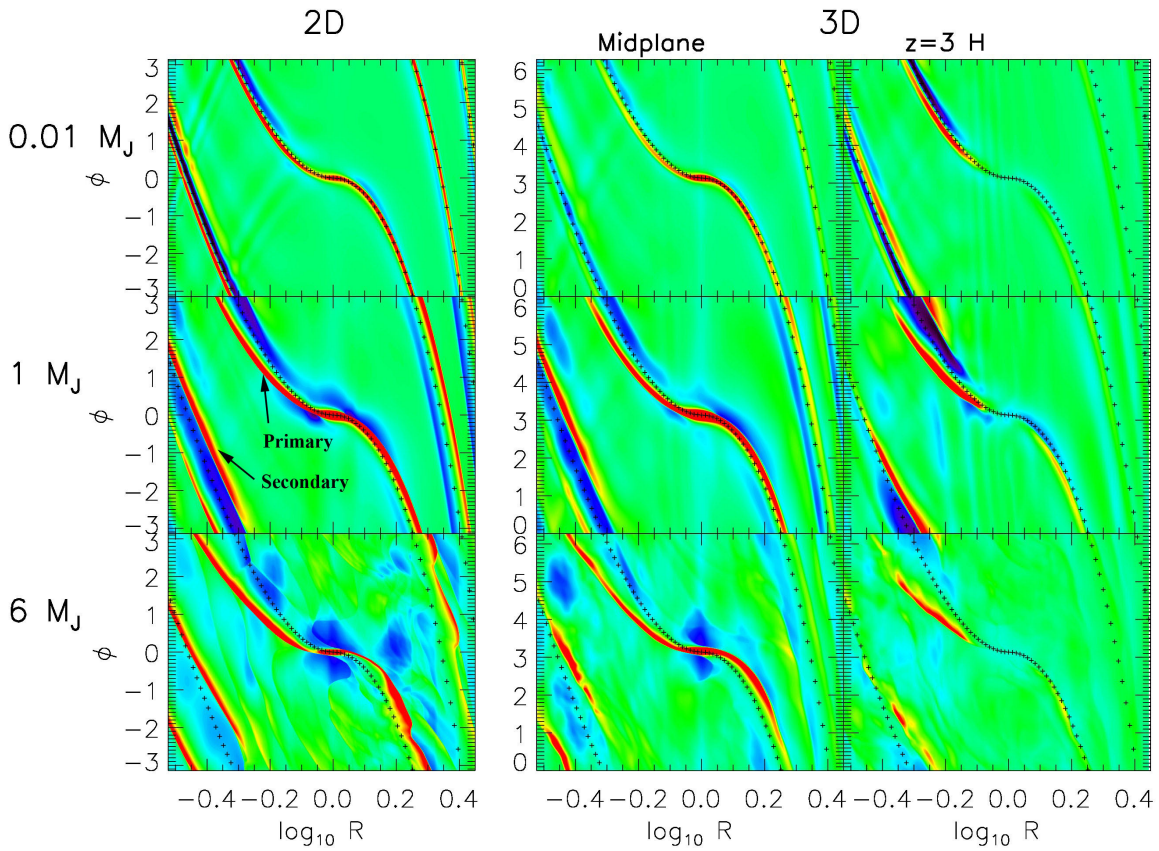

FIG. 2.— $\delta\rho/\rho_0$ for CM1ISO, CM2ISO, CM3ISO (left panels), and SM1ISO, SM2ISO, SM3ISO at the disk midplane (middle panels) and $z = 3H$ (right panels). The black dotted curves are the spiral wakes from linear theory (Equation 2). When the planet is more massive, the spiral shocks have larger deviations from the prediction of linear theory. Due to the 3-D structure of the shocks, the inner spiral shocks become more open and the outer shocks become less open at $z = 3H$ compared with the shocks at the midplane. The color bar is uniform but it has different scale in each plot to highlight the shock structure.

shocks immediately around the planet, and the shape of spiral shocks can deviate from the trajectory predicted by Equation (2) significantly. Shocks excited by a more massive planet deviate from linear theory more and their

pitch angles are larger. As shown in Figure 2), spiral shocks in the 6 M_J cases (bottom panels) are more open and deviate from the prediction of linear theory (dotted curves) more than shocks in the 1 M_J cases (middle pan-

els). The deviation from the linear theory has also been seen in previous simulations, e.g., Figure 2 and 10 of de Val-Borro et al. (2006), but it has not been explored and the physical reason for the deviation is left to be unexplained.

This deviation from linear theory shown in Figure 2 is consistent with the predictions from the weakly non-linear density wave theory by Goodman & Rafikov (2001) and Rafikov (2002). In weakly non-linear theory, the spiral shock can expand in both azimuthal directions away from Equation (2), and, at each radius, the shock density profile along the azimuthal direction is N-shaped (Figure 2 in Goodman & Rafikov 2001). The N-shaped shock profile expands in the azimuthal direction at a speed which is proportional to the normalized amplitude of the shock $((\Sigma_{shock} - \Sigma_0)/\Sigma_0)$. Thus, the higher is the planet mass, the stronger are the shocks and these shocks expand faster away from Equation (2). Then, the spiral shock has a larger pitch angle as a result.

Similar to the 0.01 M_J case, the inner spiral shocks are even more open at $z = 3H$ than at the midplane, while the outer arms become less open at the disk surface. For outer spiral arms, this 3-D effect compensates the increased pitch angel due to the shock expansion, and coincidently the outer arms almost overlap with the prediction from linear theory.

Another important feature shown in Figure 2 is that, besides the primary inner arm which originates from the planet, a secondary inner spiral arm appears with some azimuthal shift from the primary arm. This two spiral arm structure has also been seen in previous simulations having massive planets, e.g. Figure 2 in Kley (1999) and Figure 10 of de Val-Borro et al. (2006). However, it has hardly been explored in earlier simulations. Figure 2 shows that, even with a very low mass planet (0.01 M_J, the upper panels of Figure 2), another density peak (the secondary arm) emerges close to the primary inner arm with low density region (the rarefaction wave of the primary arm) in between. After the secondary arm is excited, it can become shock during the propagation and later it will become N-shaped which is similar to the primary arm. For 0.01 M_J cases, the primary and secondary arms are separated by $\delta\phi \sim 1$ at $R = 0.3$. When the planet gets more massive, the secondary arm is excited earlier and the separation between the primary and secondary arm increases. In 1 M_J cases, the two inner arms are roughly separated by $\delta\phi \sim 2$, and in 6 M_J cases, the two arms are roughly separated by $\delta\phi \sim 3$. This has an important application that we can use the separation between two arms to estimate the mass of the embedded planet. The secondary arms also have 3-D structure, they seem to be stronger and closer to the planet at the disk surface. For outer arms, the secondary arm also appears in disks having a massive planet, but the secondary outer arm is less apparent than the primary outer arm. More discussions on the 3-D structure of secondary arms will be presented in §5.

Spiral wakes/shocks are slightly more open in a disk whose EoS is not isothermal (Figure 3). This is because density waves propagate slightly faster in a fluid with a non-isothermal EoS than in a fluid at the same temperature with the isothermal EoS. In Figure 3, even with a moderate cooling rate ($T_{cool} = 1$), the spiral wakes excited by a low mass planet (0.01 M_J) can only be

fitted by Equation (2) with a larger disk scale height that is calculated with the adiabatic sound speed instead of the isothermal sound speed ($h_p = c_{s,adi}/R\Omega = \sqrt{\gamma}c_{s,iso}/R\Omega$). Other aspects of the spiral shocks in non-isothermal cases are similar to the isothermal cases, e.g., a higher mass planet excites a more open spiral shock, and the inner spiral shocks become slightly more open at higher altitudes.

To illustrate the shape of the spiral shocks in the physical space, we plot the relative density perturbation in Cartesian coordinates in Figure 4. Clearly, the more massive the planet is, the more the spiral shocks deviate from linear theory. Two well separated inner arms are also apparent when the planet mass is large, and the separation between these two arms is larger when the planet is more massive (comparing the middle and bottom panels in Figure 4).

To see how successful the weakly non-linear density wave theory of Goodman & Rafikov (2001) and Rafikov (2002) fits the shape of the shocks in simulations, we plot in Figure 5 the density profiles along the azimuthal direction at $R = 0.3, 0.5, 1.5$ and 2 for run CM1ISO. Following Goodman & Rafikov (2001) and Rafikov (2002), the density profiles have been shifted so that $\phi' = 0$ corresponds to the wake position from linear theory (black curve in Figure 5 or Equation 2). The density profiles clearly show that the shocks are N-shaped. A rarefaction wave follows the shock front and the $\delta\rho$ there can be negative before it merges to the background flow. The shock fronts deviate from $\phi' = 0$, and due to the shock expansion, the deviation is larger when the shock is further away from the planet. In the shearing-sheet approximation, the amplitude and width of the N-shaped shock scale as $|R - R_p|^{-5/4}$ and $|R - R_p|^{5/4}$ at $|R - R_p| \gg 0$ based on the weakly non-linear density wave theory of Goodman & Rafikov (2001). In a global disk spanning a range of radii, the amplitude and width of the N-shaped shock scale as $t^{-1/2}$ and $t^{1/2}$, where t is given in Equation 43 of Rafikov (2002). For our disk parameters, we have

$$ t \propto \left| \int_1^{R/R_p} |s^{3/2} - 1|^{3/2} s^{-13/8} ds \right|. \qquad (17) $$

Thus, we expect that in our global simulations the azimuthal deviation of the shock front[7] from the path predicted by Equation 2 should also scales as $t^{1/2}$.

To test this prediction, we have measured the shock positions at $R = 0.5$ and 1.5 in Figure 5, which are $\phi' = -0.9$ and 0.43 respectively. These two positions are labeled as the dashed lines in $R = 0.5$ and 1.5 panels. Then we calculate the shock positions at $R = 0.3$ and 2 to be -1.7 and 0.9, using their positions at $R = 0.5$ and 1.5 together with the scaling relationship $t^{1/2}$ where t at $R=0.3, 0.5, 1.5$, and 2 are calculated from Equation 17. These predicted shock positions are labeled as the dashed lines in $R = 0.3$ and 2 panels. We can see that they agree with the actual shock positions in the simulation very well. This confirms that the shock positions are determined by the non-linear expansion of spiral shocks. Using the same approach, we have calculated the

---

[7] In non-linear theory, the middle point of the N-shaped shock is not exactly at ϕ'=0 but it is close to ϕ'=0.
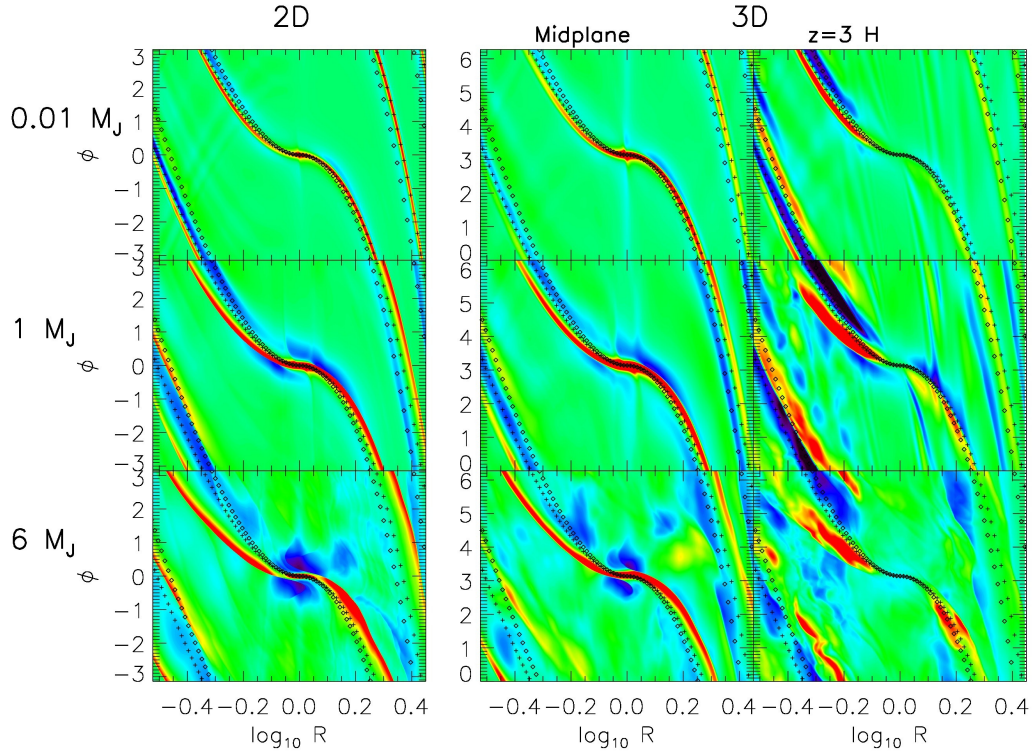
FIG. 3.— The same as Figure 2 but for CM1T1, CM2T1, CM3T1 (left panels), and SM1T1, SM2T1, SM3T1. The black squared dots represent the linear theory using isothermal sound speed while the black plus sign dots use the adiabatic sound speed.
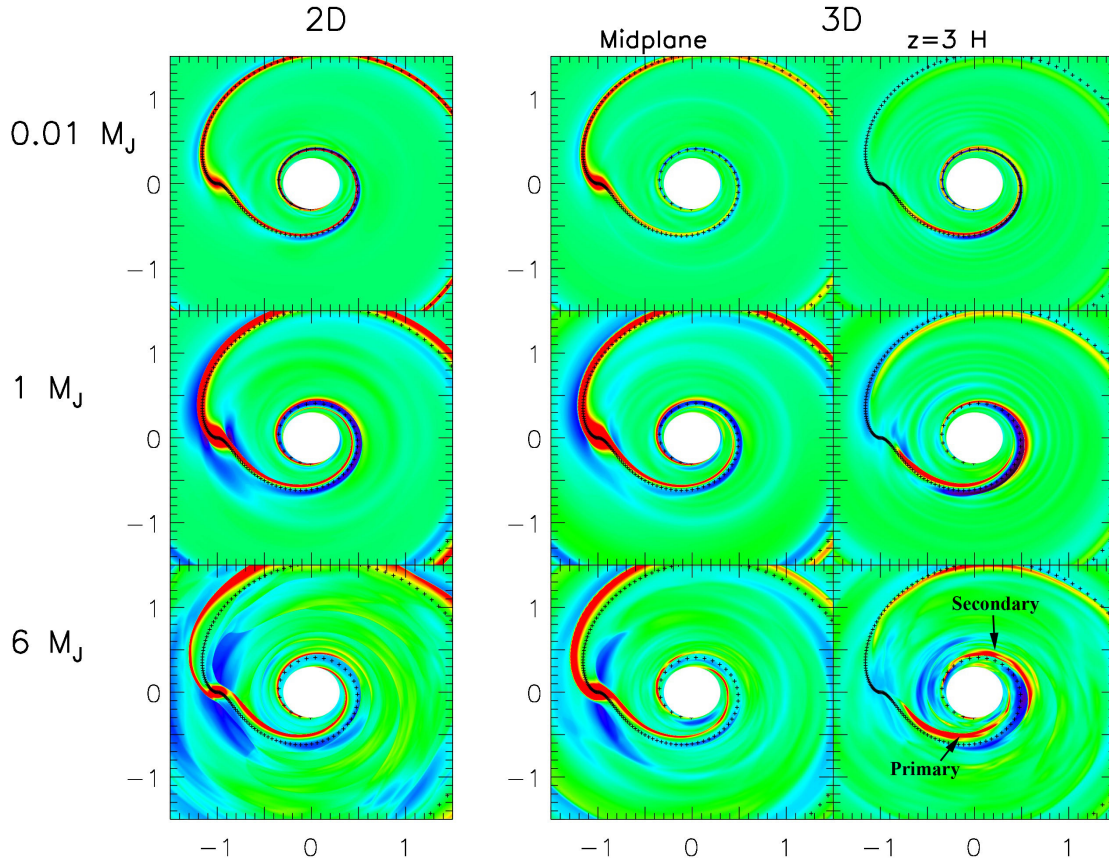

FIG. 4.— The same as Figure 2 but in Cartesian coordinates.

non-linear shock position at every radius for $R < 1$ and $R > 1$ with the normalization based on shock positions

at $R = 0.5$ and 1.5. This new predicted shock shape is plotted as the dotted curve in the left panel of Figure
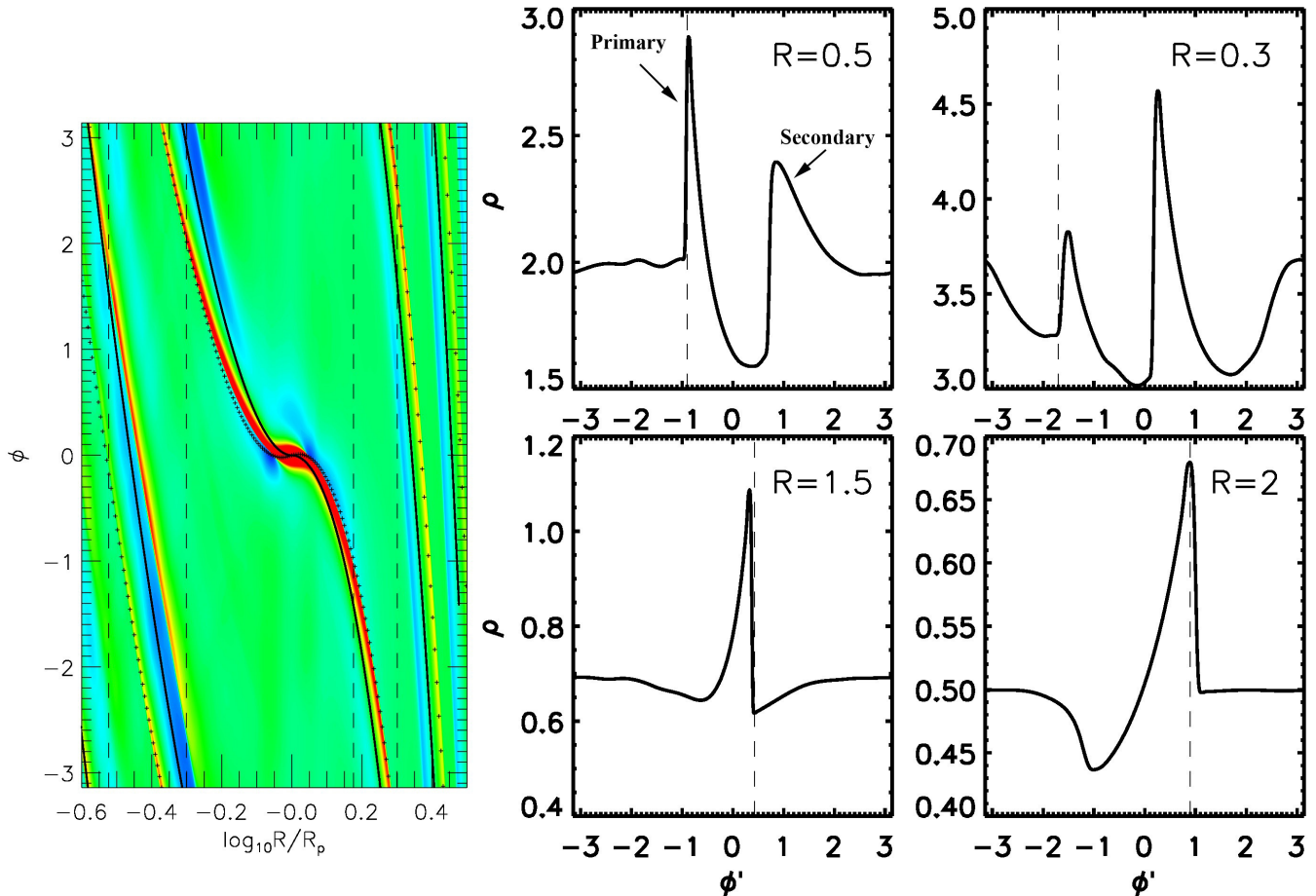
FIG. 5.— $\delta\rho/\rho_0$ for CM1ISO (left color panel) and density cuts across the ϕ direction at $R =0.5$, 0.3, 1.5, and 2.0. The solid black curve in the left color panel labels the shock position from linear theory (Equation 2). In the density cut plots, the density profile has been shifted so that the shock position from linear theory is at $\phi' = 0$. The dashed lines in $R=0.5$ and 1.5 plots label the shock fronts, while the dashed lines in $R=0.3$ and 2 plots label the predicted shock fronts from weakly nonlinear theory. In the left color contour panel, the predicted shock front from nonlinear theory is labeled as the dotted curve.

5. Despite some offset at R close to the planet, which is expected since the simple relationship $t^{-1/2}$ holds only when $|R - R_p| \gg 0$, a good agreement has been achieved between the non-linear density wave theory and the simulations. Note that in this comparison, we did not calculate the shock strength directly from non-linear theory and compare its amplitude with simulations, instead we use the scaling relationship to verify the propagation of the shock. In future, direct comparison is desired when we have a better non-linear theory which can calculate the shock excitation directly.

Although the primary arm can be fitted by the weakly non-linear density wave theory, the excitation of the secondary arm still lacks a good theoretical explanation. It may be related to the low m mode (e.g. $m = 2$, similar to disks in binary systems) or some non-linear wave coupling. Figure 5 suggests that a secondary spiral arm is excited at the other end of the N-shaped primary shock (the $R = 0.5$ panel). After it is excited, it steepens to shocks and becomes another N-shaped shock later (the $R = 0.3$ panel). Its shock front can even travel into the rarefaction wave of the primary arm (e.g. in the $R = 0.3$ panel, the secondary shock is almost at $\phi'=0$ where the rarefaction wave of the primary arm should reside.). Unlike the primary arm which already dissipates when it

travels inward from $R = 0.5$ to 0.3, this secondary arm is excited later and becomes stronger from $R = 0.5$ to 0.3. At $R = 0.3$, the secondary arm is even stronger than the primary arm. By comparing $R = 0.5$ and $R = 0.3$ panels, we also notice that the secondary arm almost keeps the same azimuthal separation with the primary arm ($\Delta\theta' \sim 1.7$) during its propagation.

5. THE 3-D STRUCTURE OF SPIRAL WAKES

Since near-IR scattered light observations only probe the shape of the disk surface, 3-D structure of spiral shocks can affect the observational signatures of these spiral shocks. Intuitively, we would expect that the spiral shocks have complicated 3-D structure. First, the wave excitation must have 3-D structure since, at the same R in the disk, the distance between the planet and the disk surface is larger than the distance at the midplane, and the force is thus weaker at the disk surface. Second, the wave propagation may have 3-D structure considering the disk becomes thinner at smaller R. Waves/shocks are more converged when they propagate inwards. They can also channel to the disk surface (Lubow & Ogilvie 1998), and, during their propagation from the high density region (e.g., the midplane) to the low density region (e.g., the disk surface), the amplitudes of perturbations have to increase to conserve the wave action.
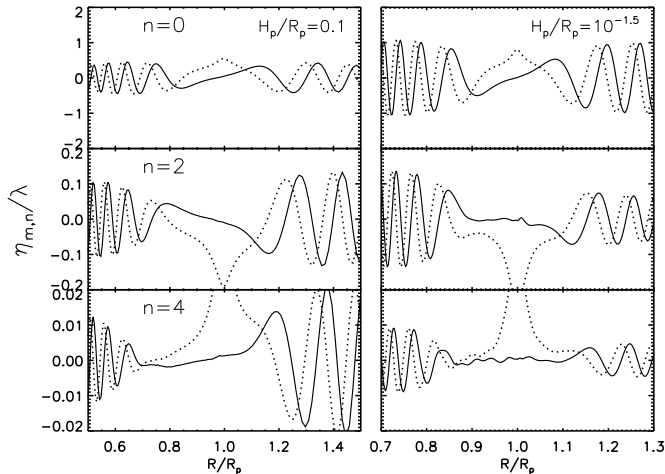
FIG. 6.— Waves excited on a 3-D disk by a low mass planet in run SM1ISO (left panels) and STHIN (right panels). Density perturbations with $n = 0, 2$, and 4 Hermite components for the m=10 Fourier mode are displayed. The real (imaginary) part of η is shown with a dotted (solid) curve. Y-scales are different for different n modes.

Since the amplitudes of perturbations determine when the waves will break into shocks, the dissipation can also be quite different between the surface and the midplane. All these effects can contribute to the 3-D structure of spiral waves/shocks.

Due to these complicated effects, it is difficult to develop an analytic theory to study the planet-induced 3-D shock structure, and we rely on numerical simulations to study such structure. However, before delving into the highly nonlinear shock regime, we can use the linear theory developed in Tanaka, Takeuchi & Ward (2002) to estimate the 3-D effect of the density waves. Following their theory for locally isothermal disks, the structure of the waves in the z direction can be studied with Hermite polynomials ($H_n(Z)$). We first expand perturbed quantities (η) from our simulations into Fourier series

$$\eta = \sum_m \mathrm{Re} \left[\eta_m e^{im(\phi - \Omega_p t)} \right] , \qquad (18)$$

where the Fourier components η_m are complex functions of R and z. Then, η_m can be further expanded with Hermite polynomials in the z direction,

$$\eta = \sum_{m=0}^{\infty} \sum_{n=0}^{\infty} \mathrm{Re} \left[\eta_{m,n} H_n(Z) e^{im(\phi - \Omega_p t)} \right] , \qquad (19)$$

where Z is the normalized height as $Z = z/H(R)$, and the first three Hermite polynomials are

$$H_0(Z) = 1 , \quad H_1(Z) = Z , \quad H_2(Z) = Z^2 - 1 . \quad (20)$$

By using the normal orthogonal relation between H_n, we have

$$\eta_{m,n} = \frac{1}{\sqrt{2\pi}n!} \int_{-\infty}^{\infty} e^{-Z^2/2} H_n(Z) \eta_m dZ . \qquad (21)$$

We can use $\eta_{m,n}$ at different n to estimate the relative importance of different Hermite components. To compare with Figure 2 in Tanaka et al. (2002), we show $m = 10$, $n = 0, 2, 4$ Fourier-Hermite components for the

perturbed density $(\delta\rho/\rho_0)$[8] in Figure 6. With the same parameters, the right panel of Figure 6 is very similar to Figure 2 in Tanaka et al. (2012). By comparing the right and left panels of Figure 6, we find that the 3-D structure is more significant in a thicker disk. The ratio between the n=2 component and n=0 component is larger in a thicker disk.

Figure 6 suggests that higher order vertical components can dominate the disk structure at the atmosphere. Although it shows that the $n = 4$ component is 10 times weaker than the $n = 2$ component, and the $n = 2$ component is 10 times weaker than the $n = 0$ component, which led Tanaka et al. (2002) to conclude that most of the angular momentum that is excited by the planet will be carried by two dimensional free waves ($n = 0$), the base function (Hermite polynomials) at $z = 3H$ gets ~ 10 times larger sequentially from H_0 to H_2 and to H_4. Thus, $\eta_{10,2}H_2$ and $\eta_{10,4}H_4$ are still comparable with $\eta_{10,0}H_0$. The density structure at the disk atmosphere can be significantly affected by higher order vertical modes.
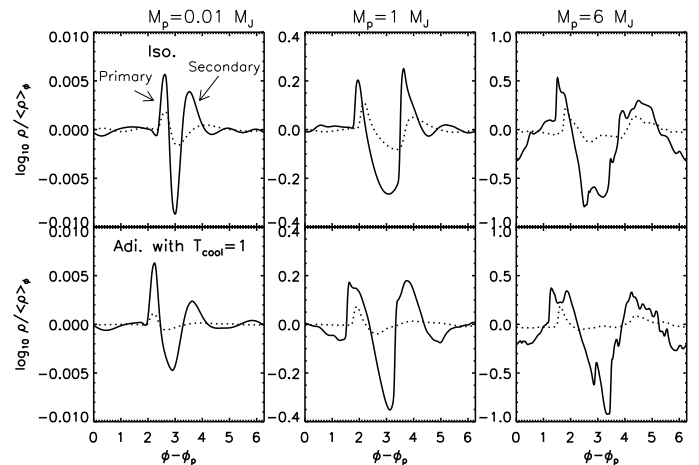

FIG. 7.— At the disk radius of $R = 0.5$, density profiles along the azimuthal direction at the disk midplane (dotted curves) and $z = 3H$ (solid curves). Simulations with different planet masses (different columns) and equations of state (upper panels: isothermal, bottom panels: adiabatic with $T_{cool} = 1$) have been shown.

Although the modal analysis is useful to verify numerical simulations and can be suggestive on the relative amplitudes of various modes, it is the 3-D structure in the real space that determines the observational signatures of waves/shocks.

By studying the shock structure in real space, we first find that the 3-D shock structure is dramatically different between inner and outer arms. For the inner arms, the density perturbation of the shock is much larger at the disk surface than at the disk midplane. The 3-D structure of the inner spiral arms at $R = 0.5$ is shown in Figure 7. At $R = 0.5$ and $z = 3H$ (solid curves), the differences between the maximum and minimum density in the logarithmic scale are 0.015, 0.4, and 1.3 for M1, M2, and M3 cases respectively, in comparison with 0.004, 0.2, and 0.4 at the disk midplane (dotted curves). The position of the wakes in non-isothermal disks (lower panels)

---

[8] Since the disk is isothermal locally, the density perturbation is quite similar to the enthalpy perturbation, and can be compared with Figure 2 in Tanaka et al. (2012).

are at smaller $\phi - \phi_p$ compared with those in isothermal disks (upper panels) at $R = 0.5$. As discussed in §4, this is due to the faster sound speed in non-isothermal disks, and the wakes are more open in these disks.
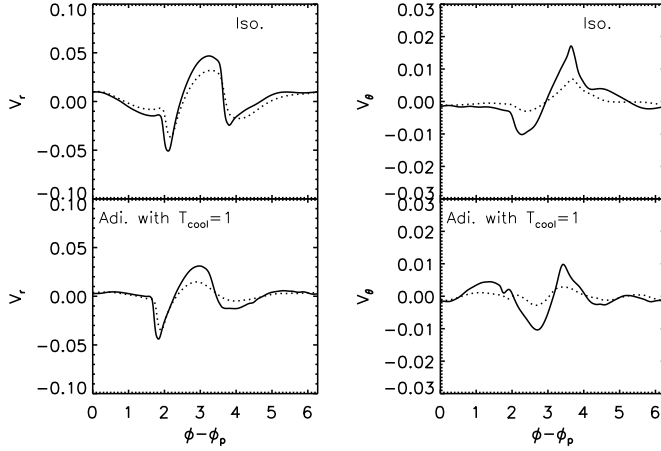

FIG. 8.— v_r (left panels) and v_θ (right panels) at $z = 1H$ (dotted curves) and $2H$ (solid curves) for SM1ISO (upper panels) and SM1T1 (bottom panels). v_θ is positive when the motion is towards the disk surface.

The secondary inner spiral arms/shocks are also more prominent at the disk surface than at the disk midplane. At the disk midplane, the secondary arms have lower amplitudes compared with the primary arms (dotted curves in Figure 7), while at $z = 3H$, the secondary arms have almost the same amplitudes as the primary arms (solid curves). The large amplitude of primary and secondary inner arms at the disk surface is due to the corrugated motion in the v_θ direction. In Figure 7 which is in the corotating frame with the planet, the disk material flows in the direction from the left side to the right side of the figure. Before meeting with the shock, the disk is in vertical hydrostatic equilibrium with the background density and $v_\theta = 0$ (Figure 8). After the shock, the disk material loses angular momentum and moves inwards with $v_r < 0$ (Figure 8). At the same time, v_θ also becomes negative, compressing the disk material at the midplane. This downward motion decreases the density of the rarefaction wave at $z = 3H$. Before meeting the secondary shock, v_θ starts to increase and becomes positive, leading to a higher density at the disk surface. At the secondary shock, v_θ reaches the maximum positive velocity and leads to the highest density at the disk surface for the secondary shock. This corrugated motion, first negative and then positive v_θ, leads to an enhanced contrast between the spiral shock and the rarefaction wave after the shock.

On the other hand, the outer spiral arms do not show a higher density perturbation at the disk surface, especially for isothermal disks, as shown in Figure 9. At $R = 2$, regardless of height, the differences between the maximum and minimum density in the logarithmic scale are both 0.002 for SM1ISO, 0.1 for SM2ISO , and 0.3 for SM3ISO. This lack of vertical variation is also reflected in Figure 10 where v_θ is very small compared with v_r (v_θ is almost two orders of magnitude smaller than v_r). Thus, the density structure of the shock is mainly determined
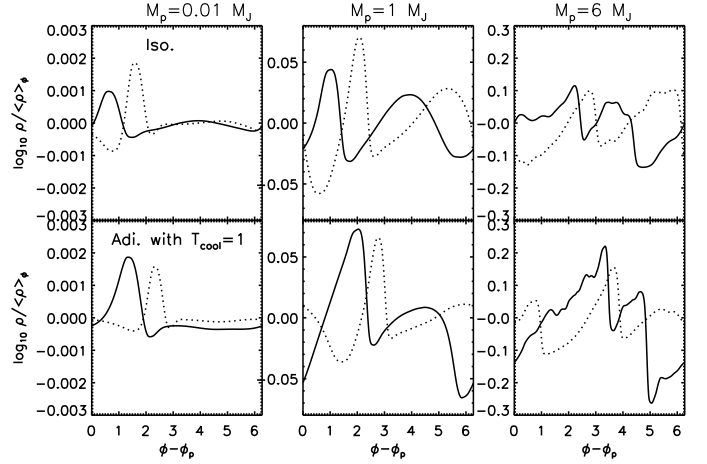

FIG. 9.— Similar to Figure 7, but at $R = 2$.
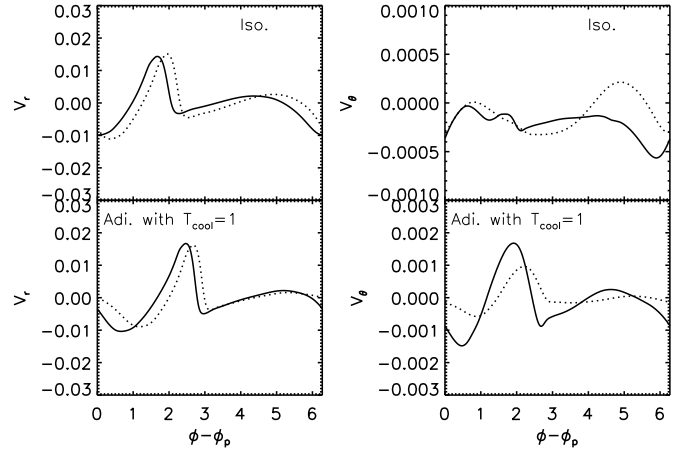
by v_r and v_ϕ due to the shock compression.

FIG. 10.— Similar to Figure 8, but at $R = 2$.

For the outer arms in non-isothermal runs (bottom panels in Figure 9), the density perturbation at the disk surface is slightly higher than the perturbation at the disk midplane. Disk material flows from the right hand side to the left hand side in Figure 9 and 10. When it meets the shock, it develops a v_θ towards the disk surface, which enhances the density at the disk surface. Although it is tempting to contribute such difference between isothermal and non-isothermal runs to the hydraulic jumps (shock bores) (Boley & Durisen 2006), such disk structure also appears even in the linear regime for the 0.01 M_J case, implying that it may be related to the eigenfunctions of the 3-D waves excited by the planet.

Finally, to illustrate the increase of the density perturbation with height and the qualitative difference between inner and outer arms, we plot the relative density perturbation along the radius at different heights ($z = 0, 1, 2, 3, 4\ H$) in Figures 11 and 12. The relative density perturbation is defined as $\rho_{max}(R, z)/\rho_{min}(R, z) - 1$, where $\rho_{max}(R, z)$ and $\rho_{min}(R, z)$ are the maximum and minimum density along the azimuthal direction ($\phi = [0, 2\pi]$) at the fixed R and z. We can see that the inner arms and outer arms are qualitatively different. For inner
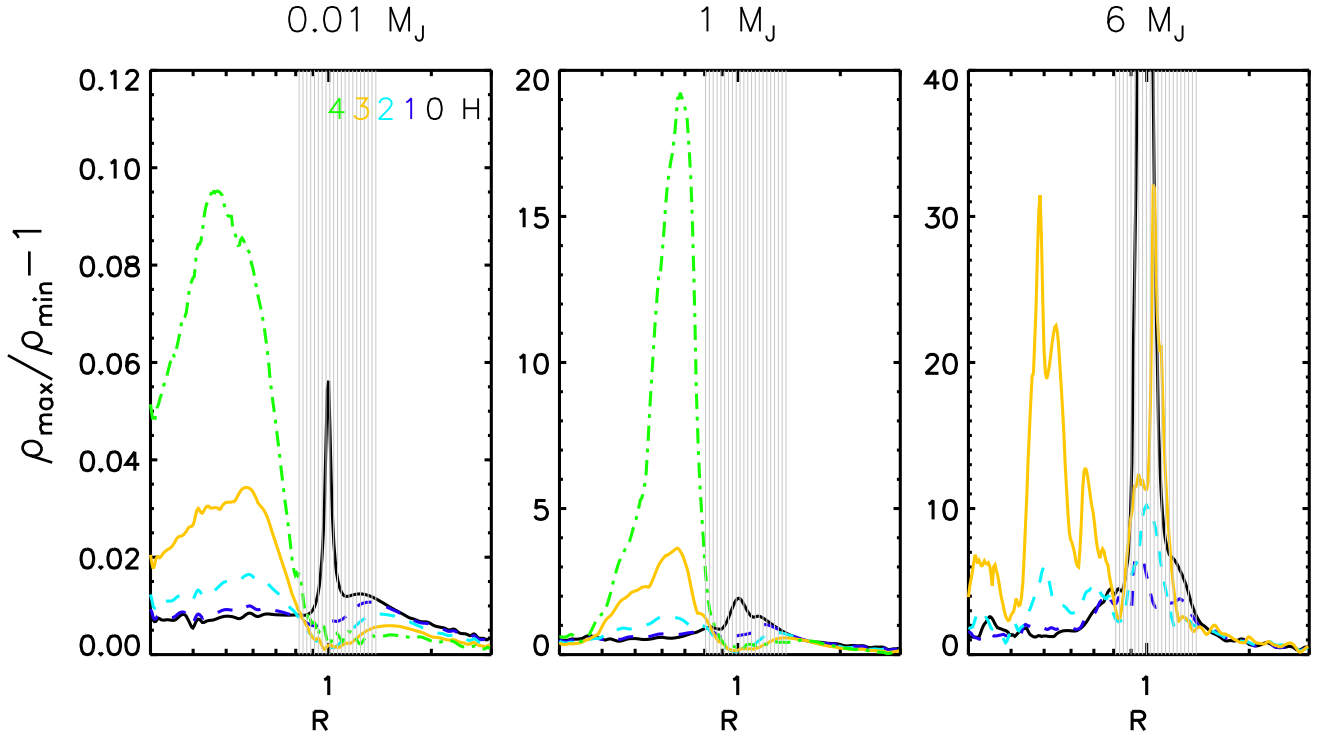
FIG. 11.— Relative density perturbations at different heights for SM1ISO, SM2ISO, SM3ISO. ρ_{max} and ρ_{min} are the maximum and minimum density along the circle in the azimuthal direction at given R and z. The black (blue, cyan, orange, green) curve is calculated at the disk midplane ($1H$, $2H$, $3H$, $4H$). The shaded region represents the region where the density perturbation is determined by the planet and the circumplanetary region instead of the spiral shock.
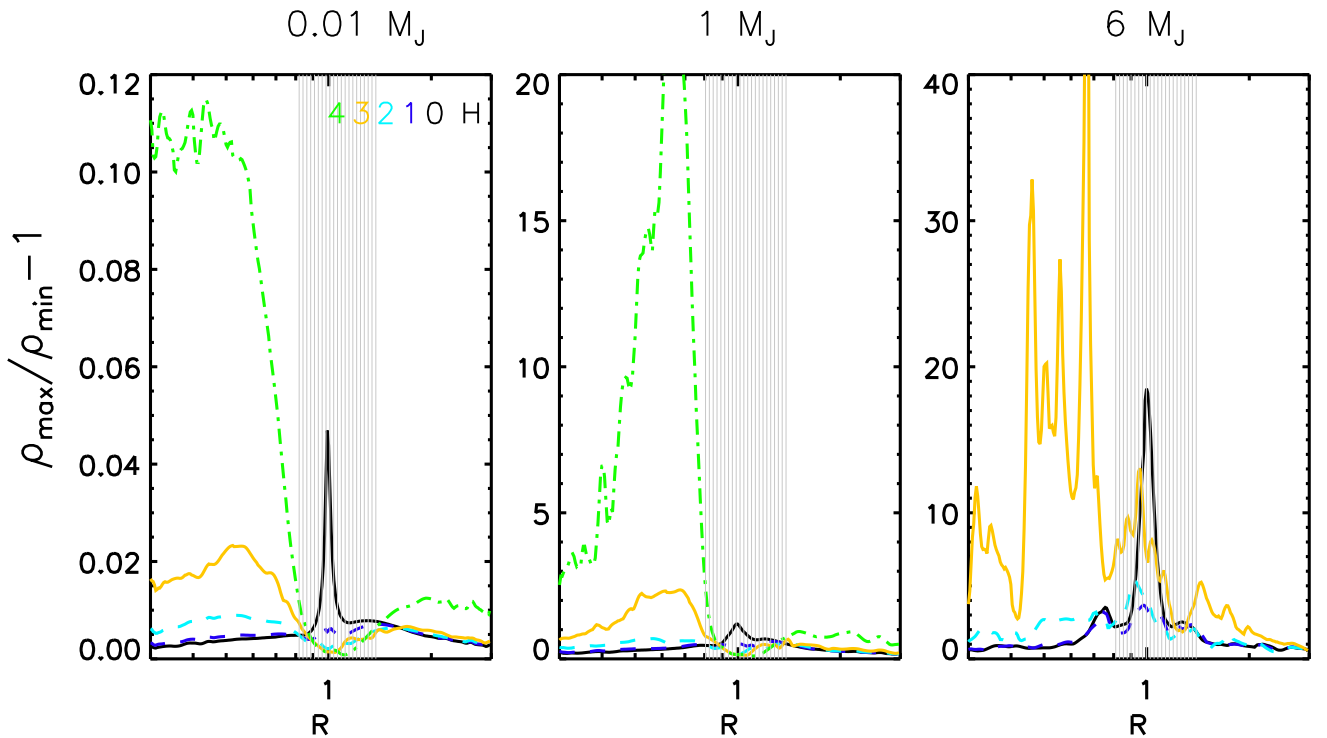

FIG. 12.— Similar to Figure 11 but for SM1T1, SM2T1, and SM3T1.

arms, the relative density perturbation is getting larger at higher altitudes, and the perturbation can increase by

more than a factor of 10 from the midplane to the disk surface. For the outer arms, the relative density pertur-

bation is almost unchanged between the midplane and the disk surface in isothermal disks (Figure 11) and only increases slightly from the midplane to the disk surface in non-isothermal disks (Figure 12). Overall, for the inner arms, the large density perturbation at the disk surface has a significant effect on the near-IR observations as shown below.

6. DISCUSSION

6.1. *Near-IR Images*

To understand how the 3-D structure of density waves/shocks affects observations, we post-process our hydrodynamical simulations with Monte-Carlo radiative transfer calculations to generate near-IR scattered light images (Figures 13 and 14). The details on the Monte-Carlo radiative transfer calculations are presented in Dong et al. (2014, 2015). To assign physical scales to our simulations, we assume that the planet is at 50 AU and the central source is a typical Herbig Ae/Be star with a temperature of 10^4 K and a radius of $2R_\odot$. ISM dust grains have been used and their distribution is assumed to follow the gas distribution. The total mass of the ISM dust is assumed to be $2 \times 10^{-5} M_\odot$. In MCRT simulations, photons from the central star are absorbed/reemitted or scattered by the dust in the surrounding disk. Full resolution polarized intensity images at H band in Figures 13 and 14 are convolved by a Gaussian point spread function with a full width half maximum (FWHM) of 0.06" to get the convolved images in Figures 13 and 14. This resolution is comparable with NIR direct imaging observations using Subaru, VLT, and Gemini. In the right two panels of Figures 13 and 14, we assume that the object is 140 pc away, while in the left two panels we assume that the distance is 70 pc so that the inner arms are shown more clearly.

To highlight the importance of the 3-D wave structure, we have also computed models by only using the disk midplane density from simulations, which is labeled as 2D→3D. In these models, we assume that the disk is in vertical hydrostatic equilibrium and puff up the midplane density to higher altitudes.

Overall, in 3D models, the inner arms are considerably more prominent than the outer arms, and normally a secondary arm can be as bright as the primary arm. The shape of the inner arms clearly deviate from the prediction of linear theory. As expected from the non-linear expansion of spiral shocks, the pitch angle of the inner spiral arms in the more massive planet case (SM6ISO, Figure 14) is larger than those in the less massive planet case (SM1ISO , Figure 13). The inner arms are also quite sharp, while the outer arms are quite broad and sometimes indistinguishable from the background disk. This difference is partly because the sharp shock fronts are facing the star for the inner arms, while they are facing away from the star for the outer arms. We calculate an approximate scattering surface, defined as the disk surface where the column density is 0.01 (in code units), for the SM3ISO model at $\phi - \phi_p = 78^o$, shown in Figure 15. Clearly, for the inner arms, the shock fronts are facing the star, while, for the outer arms, the smooth rarefaction waves are facing the star. Since the rarefaction waves change gradually with radius, they are illuminated by the star more uniformly than the shock. Thus,

the outer arms appear quite broad. However, when the planet mass is not very high (1 M_J case), the width of rarefaction waves in the radial direction can be smaller than the size of the observational beam, and we won't be able to distinguish the inner and outer arms based on the sharpness of the arms.

By comparing 3D models with 2D→3D models in Figure 13 and 14, we find that the inner spiral arms are more prominent in 3D models, as expected due to inner arms' higher density perturbation at the disk surface in 3D models (Figure 11). Even in convolved images, the polarized intensity of inner arms is at least twice stronger in 3D models than in 2D→3D models.

The secondary inner arms are as strong as the primary arms in the scattered light images, even though the primary arms have higher surface density than secondary arms. This is due to the corrugated motion discussed above in Figure 7 and 8, which increases the density of the secondary arms at the disk surface. The secondary arm is offset from the primary arm with some azimuthal angle, as also shown in the surface density plot (Figure 2). This offset is smaller in SM1ISO (Figure 13) than that in SM6ISO (Figure 14). The two spiral arms are $\sim 100^o$ apart in SM1ISO (Figure 13), while almost 180° apart in the more massive planet case (SM6ISO, Figure 14).

The outer shocks are not very apparent, and they are similar between 3D and 2D→3D models due to the outer arms having little vertical motions. As discussed in §4, the outer arms coincidentally follow linear theory (Equation 2). The secondary outer arm is also visible in Figure 14 when the planet mass is large.

Another noticeable difference between 3D and 2D→3D models is that the planet (or the circumplanetary region) is bright in 2D→3D models while it is dim in 3D models. This is because, when we puff the disk from 2-D to 3-D, we have ignored the planet's gravity so that the higher density in the circumplanetary region leads to the higher density at the disk surface. The circumplanetary region even casts a shadow to the outer disk in 2D→3D models. In realistic 3-D models, the gravity of the planet has been self-consistently included, which pulls the circumplanetary material towards the disk midplane and leads to a lower density at the disk surface. Thus, the circumplanetary region receives less irradiation by the central star, and becomes dark. On the other hand, the outer disk beyond the planet is better illuminated and thus becomes bright instead of being shadowed.

However, we need to keep in mind that we have ignored the luminosity from the planet and the circumplanetary disk in our models. Zhu (2015) point out that accreting circumplanetary disks can be very bright ($\sim 0.001\ L_\odot$ if the circumplanetary disk accepts onto Jupiter at a rate $\sim 10^{-8} M_\odot/yr$). Such high luminosity may be able to illuminate the circumplanetary region significantly. We may also be able to directly detect such accreting circumplanetary disks in direct imaging observations operating at mid-IR wavelengths.

6.2. *Thin Disks*

A realistic protoplanetary disk becomes less flared at smaller radii. To explore how the shock structure is affected by the thickness of the disk, we have shown in Figure 16 the relative density perturbation of the wakes
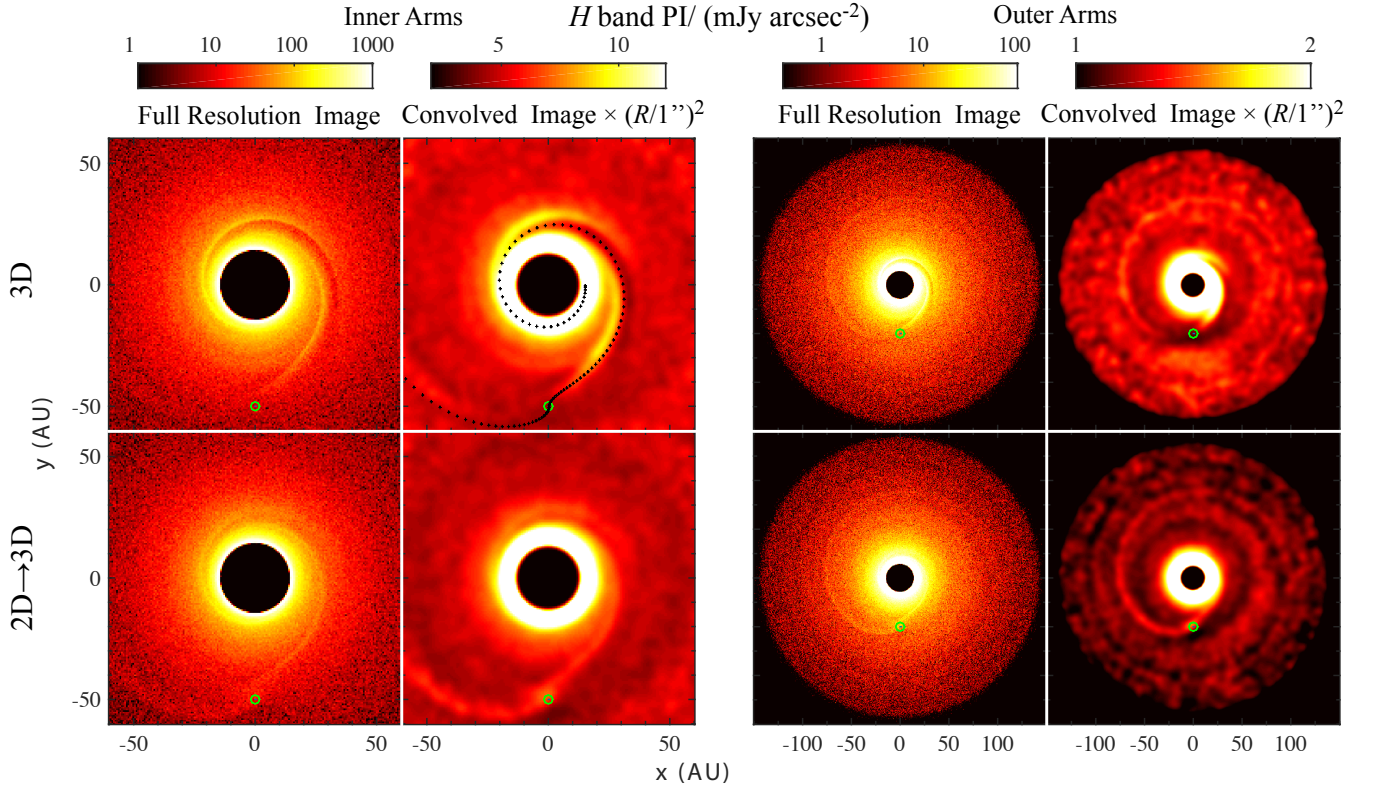
FIG. 13.— The near-IR polarized intensity maps for inner (left two panels) and outer (right two panels) arms for SM2ISO ($M_p = M_J$). The upper panels show the images using disk structure directly from 3-D simulations while the bottom panels use disk structure assuming the disk is in vertical hydrostatic equilibrium. The dotted curves are the positions of the spiral wake derived from linear theory (Equation 2).
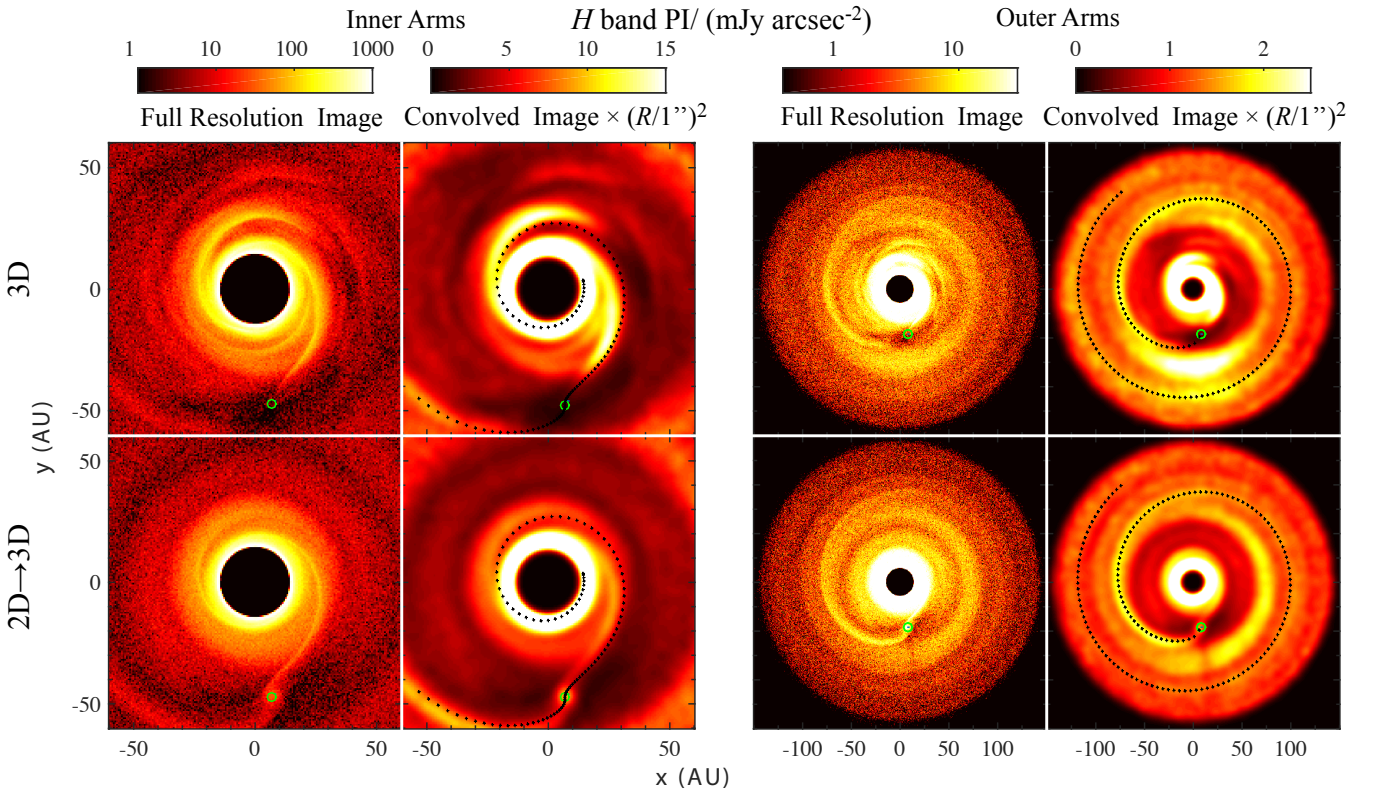

FIG. 14.— Similar to Figure 13 but for SM3ISO ($M_p = 6M_J$).

in the thin disk simulation (STHIN). Compared with Fig-   ure 11, we can see that the density perturbation increases
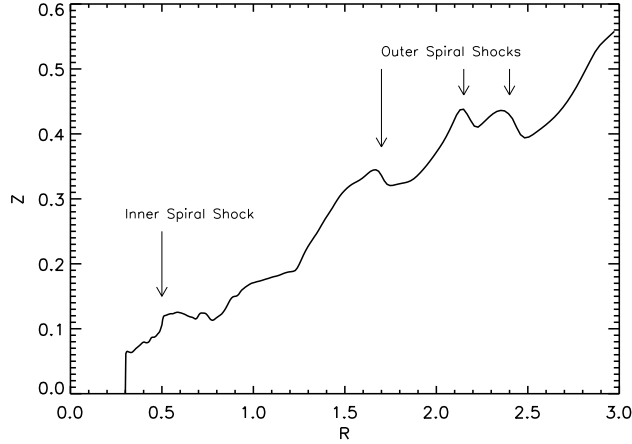
FIG. 15.— The scattering surface where the column density is 0.01 (code units) for SM3ISO. Shock fronts are facing the star for the inner spiral shocks while the rarefaction waves are facing the star for the outer spiral shocks.
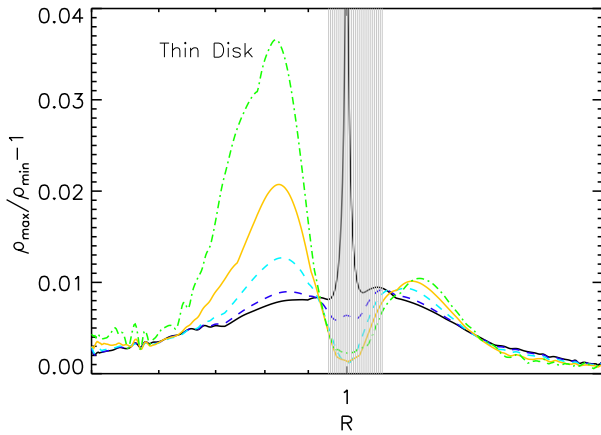

FIG. 16.— Similar to Figure 11 but for run STHIN.

by a factor of 2 from the midplane to 3 H, and a factor of 4 from the midplane to 4 H in the thin disk, compared with a factor of 4 and 10 respectively in the thick disk. This suggests that the wakes/shocks have more significant 3-D structure in a thicker disk. Although this does not favor detecting spiral arms in thinner disks (e.g. at 10 AU) in future, we need to keep in mind that the same mass planet will excite stronger density waves in a thinner disk due to its smaller thermal mass, so that the inner arms may still be observable in a thin disk.

7. CONCLUSION

We have carried out two dimensional (2-D) and three dimensional (3-D) hydrodynamical simulations to study spiral wakes/shocks excited by young planets. Simulations with different planet masses (0.01, 1, and 6 M_J) and different equations of state (isothermal and adiabatic) have been carried out.

- We find that the linear density wave theory can only explain the shape of the spiral wakes excited by a very low mass planet (e.g. 0.01 M_J). Spi-

ral shocks excited by high mass planets clearly deviate from the prediction of linear theory. For a more massive planet, the deviation is more significant and the pitch angle of the spiral arms becomes larger. This phenomenon can be nicely explained by the wake broadening from the non-linear density wave theory (Goodman & Rafikov 2001, Rafikov 2002). A more massive planet excites a stronger shock which expands more quickly, leading to a larger pitch angle.

- A secondary inner spiral arm is also excited by the planet. It seems to be excited at the edge of the N-shaped primary arm. The more massive is the planet, the larger is the separation between the primary and secondary arm. At the disk surface, the secondary inner arm can be as strong as the primary arm. The secondary inner arm almost keeps the same azimuthal separation with the primary arm at every radius in the disk.

- The spiral shocks have significant 3-D structure. They are not perpendicular to the disk midplane. They are curled towards the star at the disk surface. This further increases the pitch angle of the inner arms at the disk surface, but reduces the pitch angle of the outer arms at the disk surface. For outer arms, this effect compensates the increased pitch angle due to wake broadening. Eventually at the disk surface, the shape of outer spiral arms still roughly follows the prediction of linear theory, while the inner arms are considerably more opened than predicted by the linear theory.

- The inner spiral shocks also have significant vertical motion. The corrugated motion increases the density perturbation of the inner spiral arms by more than a factor of 10 at $z \sim 3 - 4H$ compared with the perturbation at the disk midplane. This can dramatically increase the contrast of the spiral structure in near-IR scattered light images. The outer spiral shocks have little vertical motion in isothermal disks. With a non-isothermal EoS, there are some vertical motions for the outer arms, which can make the outer arms more apparent.

- We have combined our hydrodynamical simulations with Monte-Carlo radiative transfer calculations to generate near-IR scattered light images. We find that the inner spiral arms in synthetic near-IR images using full 3-D hydrodynamical models are much more prominent than those based on 2-D models assuming hydrostatic equilibrium, as expected since for the inner arms the density perturbation at the disk surface in 3D models is much larger than that in 2D models. Inner spiral arms are prominent features that are observable by current near-IR imaging facilities. On the other hand, the outer shocks are not very apparent and they are similar in synthetic images using 3D and 2D models, since the outer arms have little vertical motions. This indicates the need to model observations (especially for inner arms) with full 3-D hydrodynamics.

- The different geometry between the inner and outer arms also affects their appearance in near-IR images. The sharp shock fronts of the inner arms face the central star directly, producing sharp narrow spiral features in observations. On the other hand, for the outer arms, the smooth rarefaction waves face the central star, producing broad and dimmer spiral features.

- In near-IR images, the circumplanetary region is very dim since the planetary gravity reduces the density at the disk atmosphere. However, the disk region behind the planet can be better illuminated and becomes bright.

- In the Appendix, we have shown that buoyancy resonances are confirmed in global adiabatic simulations even if the disk has a moderate cooling rate. They can lead to sharp density ridges around the planet, which may have observational signatures.

Overall, spiral arms (especially inner arms) excited by low mass companions are prominent features in near-IR scattered light images. Most importantly, we can use the shape of spiral patterns and the separation between the primary and secondary arms to infer not only the companion's position but its mass.

In a companion paper (Dong et al. 2015), we have combined MCRT and hydrodynamical simulations from this paper, and shown that planet-induced inner arms can explain recent near-IR direct imaging observations for SAO 206462 and MWC 758.
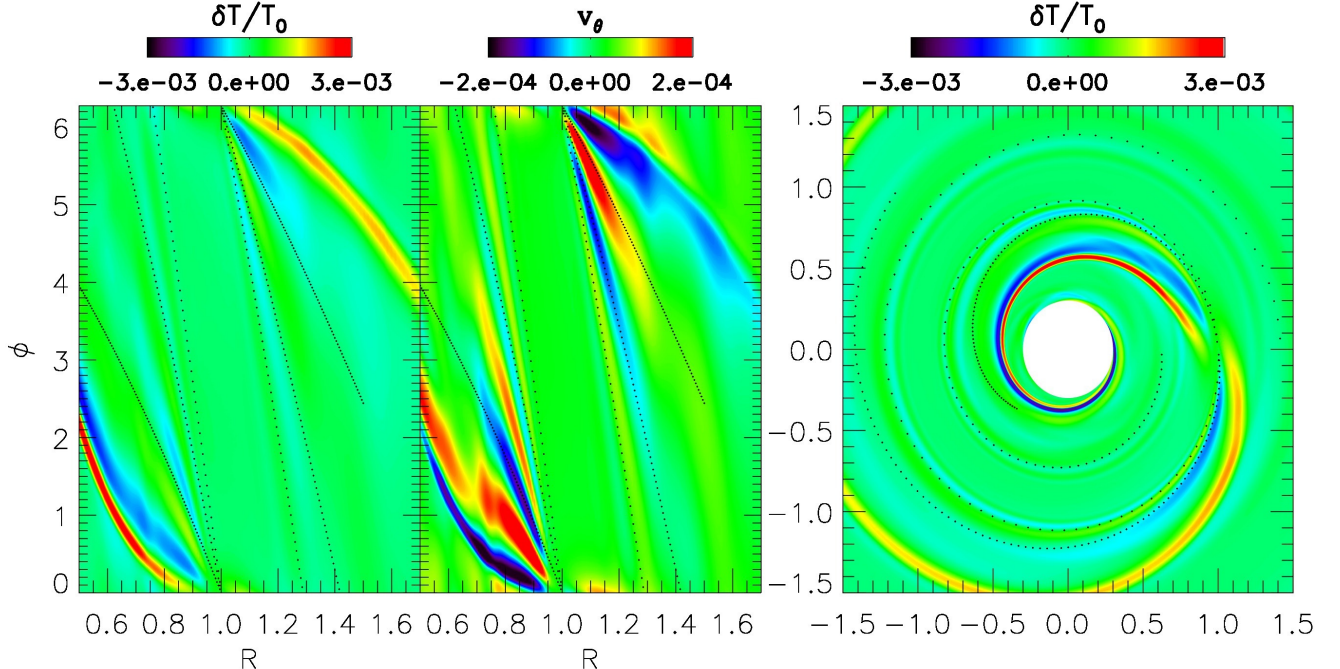
APPENDIX

BUOYANCY RESONANCES

FIG. 17.— Temperature fluctuations (the left panel) and v_θ (the middle panel) at $z = 2H$ for SM1T1. The right panel is the same as the left panel but in Cartesian coordinates. The dotted lines/curves are the position of buoyancy resonances from Equation (A3).
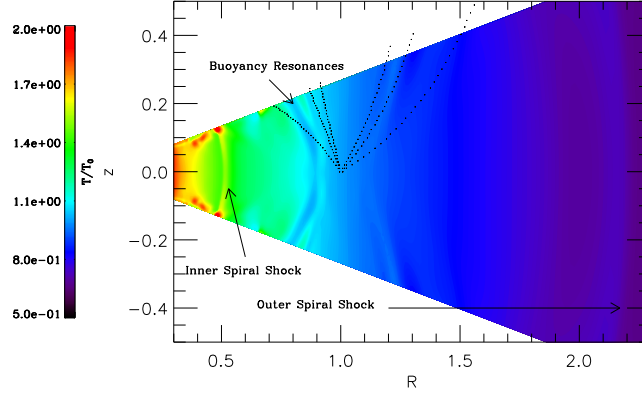
FIG. 18.— The temperature structure for SM2T1 at an azimuthal slice ($\phi - \phi_p = 100^o$). Spiral shocks and buoyancy resonances are labeled. The dotted lines are again from Equation (A3).

The inner and outer spiral shocks are due to the steepening of spiral density waves which are excited by the planet at Lindblad resonances. At Lindblad resonances, the Doppler shifted frequency matches the disk epicyclic frequency ($m(\Omega_p - \Omega) = \pm\kappa$) and density waves are excited.

However, besides the epicyclic frequency, the disk also has other natural frequencies. When the disk is not strictly isothermal, it has a non-zero Brunt-Väisälä frequency

$$N(z) = \sqrt{\frac{\gamma - 1}{\gamma} \frac{g(z)}{c_{s,iso}}} \tag{A1}$$

where $c_{s,iso}^2 = p/\rho$. Matching the Brunt-Väisälä frequency with the Doppler shifted frequency, we have

$$\sqrt{\frac{\gamma - 1}{\gamma}} \frac{\Omega_K(R)z}{H} \left(1 + \frac{z^2}{R^2}\right)^{-3/2} = \pm m(\Omega_p - \Omega). \tag{A2}$$

Given a m, Equation (A2) gives the position of the resonances. These buoyancy resonances were discovered in shearing box simulations (Zhu, Stone, & Rafikov 2012) and studied analytical in Lubow & Zhu (2014). They have significant contributions to the planetary torque, especially around the planet, which may affect planet migration. These resonances are infinitely thin, and no waves are excited to carry the deposited angular momentum and energy away. Their dissipation relies on microscopic viscosity or radiative cooling. Thin density ridges with large temperature and velocity variations appear at these resonances.

When various m modes overlap with each other, we can roughly estimate the position of the final density ridges caused by buoyancy resonances following Equation 10 and 11 in Zhu et al. (2012). First, given a m, we can calculate the corresponding resonance position at R and z. Then using the azimuthal wavelength for this mode $\lambda = 2\pi/m$, the geometric location of the constant phase $2n\pi$ (n is integer) is given by $\phi = n\lambda$ (assuming the phase of buoyancy waves is 0 at the planet position.). Thus,

$$\phi = \pm 2n\pi(\Omega_p - \Omega)\sqrt{\frac{\gamma}{\gamma - 1}} \frac{H}{\Omega_K(R)z} \left(1 + \frac{z^2}{R^2}\right)^{3/2}. \tag{A3}$$

We plot temperature fluctuations and v_θ at $z = 2H$ for SM1T1 in Figure 17. The positions of buoyancy resonances given by Equation (A3) are plotted with dotted lines/curves. Figure 17 shows that both temperature fluctuations and v_θ are nicely tracked by Equation (A3), suggesting that buoyancy resonances exist in disks even with $T_{cool} = 1$.

Even though buoyancy resonances can affect planet migration, they may not be observed through direct imaging technique since the density fluctuations caused by these resonances are much weaker than the spiral density waves excited by Lindblad resonances. For example, in the $z = 3H$ panels of Figure 3, we can see some density fluctuations close to the corotation region (especially for SM2T1, the 1 M_J case), but they are much weaker than the spiral shocks.

These buoyancy resonances also have vertical structure, as shown in Figure 18. We sliced through the disk at a fixed ϕ, and the buoyancy resonance curves are plotted as dotted curves in Figure 18. At the disk midplane, $N = 0$ and there are no buoyancy resonances. Since N increases with disk height, $|\Omega_p - \Omega|$ also needs to increase with height to match the Brunt-Väisälä frequency considering λ and m are the same at the same ϕ. Thus, the curves move away from the planet position towards the disk atmosphere.

Figure 18 also shows the inner and outer spiral shocks which are hotter at the shock position.

REFERENCES

Baruteau, C., Crida, A., Paardekooper, S.-J., et al. 2014, Protostars and Planets VI, 667

Benisty, M., Juhasz, A., Boccaletti, A., et al. 2015, A&A, 578, L6

de Val-Borro, M., Edgar, R. G., Artymowicz, P., et al. 2006, MNRAS, 370, 529

Dong, R., Rafikov, R. R., & Stone, J. M. 2011, ApJ, 741, 57

Dong, R., Zhu, Z., & Whitney, B. 2014, arXiv:1411.6063

Dong, R., Zhu, Z., Rafikov, R. R., & Stone, J. M., 2015, ArXiv

Duffell, P. C., & MacFadyen, A. I. 2012, ApJ, 755, 7

Espaillat, C., Muzerolle, J., Najita, J., et al. 2014, Protostars and Planets VI, 497

Gardiner, T. A., & Stone, J. M. 2005, Journal of Computational Physics, 205, 509

Gardiner, T. A., & Stone, J. M. 2008, Journal of Computational Physics, 227, 4123

Garufi, A., Quanz, S. P., Avenhaus, H., et al. 2013, A&A, 560, A105

Goodman, J., & Rafikov, R. R. 2001, ApJ, 552, 793

Grady, C. A., Muto, T., Hashimoto, J., et al. 2013, ApJ, 762, 48

Hubeny, I. 1990, ApJ, 351, 632

Juhász, A., Benisty, M., Pohl, A., et al. 2015, MNRAS, 451, 1147

Kley, W. 1999, MNRAS, 303, 696

Lubow, S. H., & Ogilvie, G. I. 1998, ApJ, 504, 983

Lubow, S. H., & Zhu, Z. 2014, ApJ, 785, 32

Muto, T., Grady, C. A., Hashimoto, J., et al. 2012, ApJ, 748, L22

Nelson, R. P., Gressel, O., & Umurhan, O. M. 2013, MNRAS, 435, 2610

Ogilvie, G. I., & Lubow, S. H. 2002, MNRAS, 330, 950

Rafikov, R. R. 2002, ApJ, 569, 997

Richert, A. J. W., Lyra, W., Boley, A., Mac Low, M.-M., & Turner, N. 2015, ApJ, 804, 95

Stone, J. M., Gardiner, T. A., Teuben, P., Hawley, J. F., & Simon, J. B. 2008, ApJS, 178, 137

Tanaka, H., Takeuchi, T., & Ward, W. R. 2002, ApJ, 565, 1257

Zhu, Z., Stone, J. M., & Rafikov, R. R. 2012, ApJ, 758, L42

Zhu, Z., Stone, J. M., & Rafikov, R. R. 2013, ApJ, 768, 143

Zhu, Z. 2015, ApJ, 799, 16